ROYAL SOCIETY OF CHEMISTRY

PAPER

Bulk spin-crossover in the complex [FeL(NCS)$_2$] of a tris(pyridyl)ethane-derived N$_4$-ligand—a temperature-dependent crystallographic study†

Dennis Wiedemann and Andreas Grohmann*

We have recently shown that the vacuum-deposited complex [Fe^{II}L(NCS)$_2$] (L: 1-{6-[1,1-di(pyridin-2-yl)-ethyl]-pyridin-2-yl}-*N*,*N*-dimethylmethanamine) is capable of a thermally induced spin crossover (SCO) in direct contact with a graphite surface. The SCO significantly differs from the transition behaviour in the bulk phase (powder). In the present work, the assumption of virtually no intermolecular interaction in the powder is confirmed by comparison with the spin transition in acetone solution ($T_{1/2}$ = 234[3] K, ΔT_{80} = 58[4] K), as monitored by temperature-dependent UV/Vis spectroscopy. The complex crystallises from chlorocarbons in the form of a number of pseudopolymorphs. Amongst these, the sufficiently stable solvate [Fe^{II}L(NCS)$_2$]·CHCl$_3$ is investigated by variable-temperature single-crystal X-ray diffractometry. Its SCO behaviour ($T_{1/2}$ = 240[3] K, ΔT_{80} = 35[4] K) correlates with features of molecular structure that are unambiguously identified by analysis of the tensor of thermal expansion. Following comprehensive comparison of spin-transition properties in different states of aggregation (also in relation to the newly synthesised high-spin iron(II) and iron(III) complexes [Fe^{II}Cl$_2$L] and [Fe^{III}Cl$_2$L]PF$_6$), a mode of adsorption on graphite surfaces is proposed, that complies with all previous findings.

Introduction

Spin crossover (SCO), as defined in the IUPAC "Gold Book", is a "type of molecular magnetism that is the result of electronic instability [...] caused by external constraints (temperature, pressure, or electromagnetic radiation), which induce structural changes at molecular and lattice levels".[1] The definition invokes the ability of a compound to undergo a spin-state transition in response to external stimuli (which, as we know today, can be much more diverse than stated in the definition from 1997 quoted above). In principle, SCO can occur with any 3d^4–3d^7 metal ion in pseudo-octahedral coordination.[2] Iron(II) and iron(III) complexes account for the biggest share and are most intensively studied with regard to applications in information storage and spintronics.[3–5] In these compounds, the transition takes place between the enthalpically preferred low-spin (LS) and the entropically preferred high-spin (HS) state; for Fe^{2+}/Fe^{3+}, these are the states $^1A_{1g}$/$^2T_{2g}$ (LS) and $^5T_{2g}$/$^6A_{1g}$ (HS), respectively. As subtle changes in molecular structure or solid-state arrangement can lead to dramatic changes in the switching behaviour,[6] the synthesis[7] as well as theoretical description[8] of such SCO compounds are the subject of intense current research.

Additional challenges arise from the need to transform substances into materials in order to make them useful for actual spintronic devices: the interaction with surfaces for containment or contacting increases complexity beyond design or description with common models. Further, to be able to compete, any new technology has to overcome at least some of the disadvantages or physical limits of established silicon-based electronics, *e.g.* by allowing for further miniaturisation. This has led to a growing interest in the magnetochemistry of various types of complexes on surfaces and the possibility to preserve bulk behaviour in ensembles with reduced dimensions.[9,10]

There are many examples where direct contact of a coordination compound with a surface efficiently quenches the SCO behaviour otherwise observed. For instance, electron-induced spin-state switching in ultra-high vacuum (UHV) deposited [Fe^{II}(bpb)$_2$(phen)] (bpb: bis[1*H*-pyrazol-1-yl]borate; phen: 1,10-

Institut für Chemie, Technische Universität Berlin, Straße des 17. Juni 135, 10623 Berlin, Germany. E-mail: andreas.grohmann@chem.tu-berlin.de;
Fax: +49 30 314-22935; Tel: +49 30 314-79877

†Electronic supplementary information (ESI) available: Additional figures, data of tensor analyses, CIFs of crystal structures and variable-temperature diffraction. CCDC 960951–960957. For ESI and crystallographic data in CIF or other electronic format see DOI: 10.1039/c3dt53070a
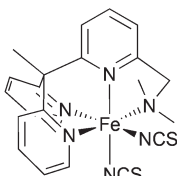
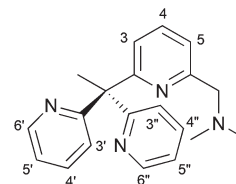**Fig. 1** Structural formula of [Fe^{II}L(NCS)$_2$] (**1**).

Fig. 2 Ligand L with hydrogen–atom numbering scheme.

phenanthroline) on Au(111) only occurs from the second molecular layer onwards.[11] Similarly, [Fe^{II}(NCS)$_2$(phen)$_2$] does not undergo SCO when adsorbed on Cu(100). The transition can, however, be induced by a tunnelling current if a layer of CuN is separating the molecules from the metal—an example of the remarkable sensitivity of molecular SCO materials towards the environment.[12]

Beyond two-dimensional arrangements like thin films, mono- or bilayers, spin-state interconversion has recently also been detected in one-dimensional chains of oligonuclear "beads" of [Fe^{II}(dptp)$_2$](BF$_4$)$_2$ (dptp: 2,6-di[1H-pyrazol-1-yl]-4-[thiocyanatomethyl]pyridine) on highly oriented pyrolytic graphite (HOPG), by current-imaging tunnelling spectroscopy (CITS).[13,14] Nanoparticles of [Fe^{II}\{(mepy)$_3$tren\}](PF$_6$)$_2$ ([mepy]$_3$-tren: tris[4-(6-methylpyridin-2-yl)-3-aza-3-butenyl]amine) may be considered as zero-dimensional entities. They show thermal SCO characteristics that differ from those of the bulk substance, and the crystallinity of the particles has a major influence on relaxation dynamics after light-induced excited spin-state trapping (LIESST).[15] Isolated molecules of [Fe^{II}\{BH$_2$(pz)$_2$\}$_2$(bipy)] (pz: 1H-pyrazol-1-yl; bipy: 2,2′-bipyridine) on Au(111) have recently been reported to be capable of temperature- and light-induced spin transitions. The important role of molecule–surface interactions has been probed by X-ray absorption spectroscopy (XAS).[16]

We have previously shown that a submonolayer of [Fe^{II}L-(NCS)$_2$] in direct contact with HOPG (**1**, L: 1-\{6-[1,1-di(pyridin-2-yl)ethyl]-pyridin-2-yl\}-N,N-dimethylmethanamine, see Fig. 1) exhibits a thermally induced, fully reversible SCO.[17] For this purpose, the substance was UHV-deposited on a freshly prepared surface at elevated temperatures and investigated using XAS. The differences between surface behaviour and bulk behaviour suggest that interactions with the substrate are more important than intermolecular forces.

Here, we report on the bulk SCO-behaviour of **1**. In our previous work we had used SQUID susceptometry to show that—like the HOPG-adsorbed submonolayer—solvent-free powders of [FeL(NCS)$_2$] (**1**) are capable of a thermally induced, reversible, gradual one-step spin crossover without hysteresis.[17] Here, we present the results of temperature-dependent solution UV/Vis spectroscopy, structure analyses and evaluation of the thermal-expansion tensor *via* single-crystal X-ray diffraction. The results shed light on the molecular changes associated with the spin-state transition in the crystalline state and help assess the role of intermolecular *vs.* molecule–substrate interactions on surfaces.

Results and discussion

Complex synthesis

[Fe^{II}L(NCS)$_2$] (**1**), [FeCl$_2$L] (**2**) and [FeCl$_2$L]PF$_6$ (**3**) are readily synthesised in high yields by addition of L to iron(II)/iron(III) chloride and (for **3**) subsequent ligand/anion exchange, using a tetrabutylammonium salt (see Scheme 1). While the SCO in **1** is the focus of the present work, HS-iron(II)/iron(III) complexes **2** and **3**, as well as the already published LS-iron(II) photosensitiser [Fe(CN)$_2$L] (**4**),[18] serve as structural models for comparison of spin-state dependent parameters.

Spin crossover in solution

The study of spin-crossover complexes in solution provides data for the dilute state. Whereas powder measurements may be influenced by intermolecular interactions, solute analyses can provide a reference model excluding them. For [FeL(NCS)$_2$] (**1**), a striking thermochromism was found in a variety of solvents like methanol, ethanol, acetone, acetonitrile, dichloromethane and chloroform. Upon cooling such solutions with liquid nitrogen, the original colour intensifies and undergoes a bathochromic shift (from orange to red), as noticed by optical inspection (see Fig. S1†). As this phenomenon—deemed to be the result of a spin-state transition—seemed to be most pronounced in acetone solutions, we investigated them further using temperature-dependent UV/Vis spectroscopy.

As incipient freezing of the solution prevented reliable measurements below *ca.* −85 °C (188 K), we recorded spectra in the temperature interval 188(1) K ≤ T ≤ 303(1) K in increments of 5 K.‡ Bands in the wavelength range of 350 nm ≤ λ ≤ 750 nm have been evaluated (see Fig. 3); prominent solvent bands prohibited the use of data below the lower limit. The bands with maxima at 400 nm and 460–470 nm are due to spin-allowed metal-to-ligand charge-transfer (MLCT). The former and the latter are due to electronic transitions into ligand-centred π^*-orbitals which are antisymmetric and symmetric with respect to a two-fold symmetry element, respectively. The less intense, broad shoulder around 600 nm is probably caused by spin-forbidden transitions into triplet states (^{1}A$_{1g}$ → ^{3}MLCT).[19,20]

With increasing temperature, the absorbance A in the Vis region decreases to about one-fifth and band positions shift

‡The spectrum at T = 258(1) K had to be excluded from subsequent calculations as it showed unrecoverable unsystematic errors in background subtraction.
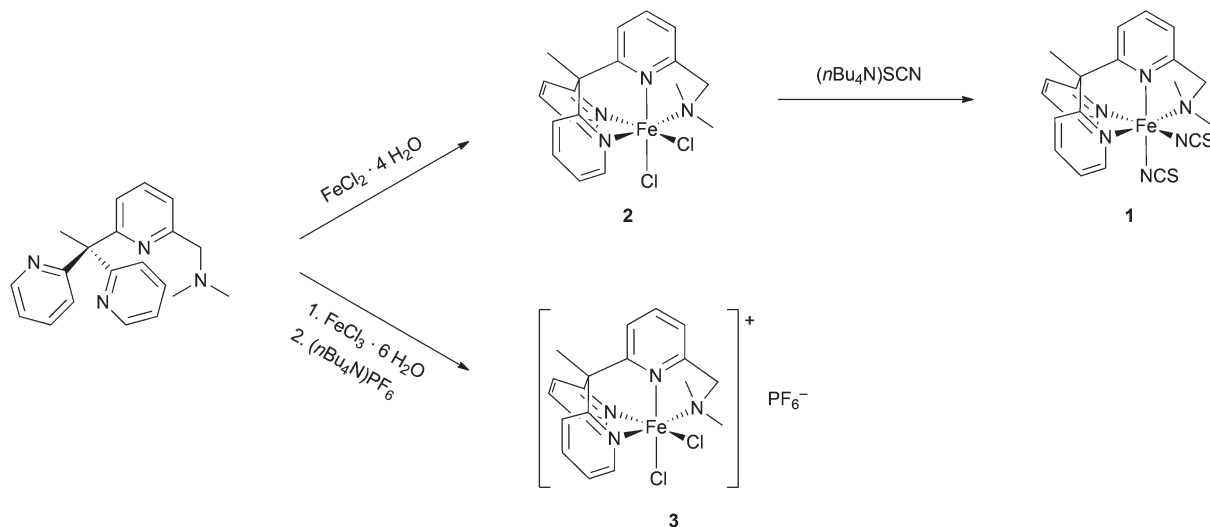
Scheme 1 Synthesis of [FeL(NCS)₂] (1), [FeCl₂L] (2) and [FeCl₂L]PF₆ (3).

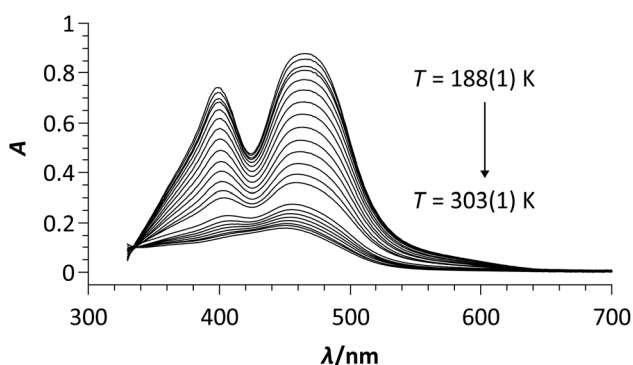**Fig. 3** Temperature-dependent UV/Vis spectra of **1** in acetone ($c =$ 0.1 mmol L^{-1}).
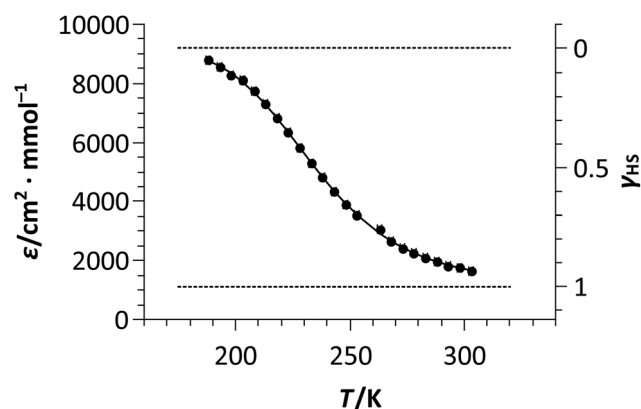
Fig. 4 Plot of the extinction coefficient (ε) and the mole fraction in the HS state (γ_{HS}) *vs.* temperature for **1** in acetone with fit of a non-interaction model (eqn (2); solid line) and extinction coefficients of the pure states (dashed lines).

slightly (*e.g.* from 466 nm to 450 nm for the absolute maximum). This behaviour is typical of a conversion from the low- to the high-spin state, the MLCT bands of which lie in the UV range (as commonly rationalised by a charge-transfer of higher energy in the HS state due to longer metal–ligand bonds).[21] An isosbestic point at 335 nm marks the boundary between the UV and Vis-MLCT regimes of **1** in acetone. This behaviour supports the notion that an SCO is responsible for the observed thermochromism—which is by no means always the case with SCO-capable compounds.[22]

The plot of the molar extinction coefficient ε at 466 nm against temperature (see Fig. 4) is of sigmoidal shape, as is expected for a spin crossover. However, the transition is incomplete in the interval examined, so that the molar extinction coefficients ε_{HS} and ε_{LS} of the pure spin states have to be determined from a fit (see eqn (1), γ_{HS}: mole fraction of molecules in the HS state).

$$\varepsilon(T) = \varepsilon_{LS} + \gamma_{HS}(T)(\varepsilon_{HS} - \varepsilon_{LS}) \quad (1)$$

On the basis of this equation, a curve (see Fig. 4) may be fitted to the data using a simple non-interaction model

derived from the reaction isotherm equation of the SCO (HS-**1** ⇌ LS-**1**) and the definition of the Gibbs energy (see eqn (2), $\Delta_{SCO}H_m$: molar SCO enthalpy, $\Delta_{SCO}S_m$: molar SCO entropy, R: universal gas constant).[17]

$$\gamma_{HS}(T) = \left[\exp\left(\frac{\Delta_{SCO}H_m}{RT} - \frac{\Delta_{SCO}S_m}{R}\right) + 1\right]^{-1} \quad (2)$$

The resulting molar extinction coefficients of the pure states, $\varepsilon_{LS} = 9200(60)$ cm^2 mmol^{-1} and $\varepsilon_{HS} = 1110(60)$ cm^2 mmol^{-1} (dashed lines in Fig. 4), are reasonable for this substance class. Rescaling with these as extrema (using eqn (1)) yields γ_{HS}.

The thermodynamic and statistical fit parameters are given in Table 6. Additionally, the broadness parameter ΔT_{80} and the (adjusted) coefficients of determination R^2 and $\bar{R}^2$ are tabulated. ΔT_{80} is defined as the difference of temperatures at which 80% of the molecules are in the HS and the LS state,

respectively, and is considered a measure of the molecular interaction during SCO.[23] The coefficients of determination can be used to judge the adequacy of the model.

The values obtained for powder and solution are similar. Thus, as in solution, intermolecular interactions in the powder of **1** seem equally absent (even if the latter fit does have a slightly lower coefficient of determination). The transition temperatures $T_{1/2}$ lie in the same range and are fairly high for this complex class. This may be due to the stereochemical constraints imposed by the ligand, which stabilise the LS state more than the HS state.

Spin crossover in the crystal

In our hands, solvent-free crystals of **1** were inaccessible from solution. Instead, the pseudopolymorphs [FeL(NCS)$_2$]·CHCl$_3$ (**1a**) and [FeL(NCS)$_2$]·2CHCl$_3$ (**1b**) co-crystallised from chloroform solutions.§ The two species could, however, be distinguished optically as they formed orange and dark red plates at r.t., respectively—a first hint at different transition temperatures for a possible SCO. To monitor the latter, temperature-dependent measurements of the cell volume V were performed (between 150 and 300 K). While crystals of **1a** were stable over the whole temperature interval, crystals of **1b** started to decompose at 260 K. Presumably, the evaporation of one equivalent of chloroform causes degradation and the appearance of powder rings in diffraction patterns.

In the low-temperature regime (150–200 K for **1a**, 150–240 K for **1b**), the data are quasi-linear and show no sign of a beginning phase transition. Thus, a standard model of thermal expansion using a temperature-independent coefficient γ of volumetric expansion was fitted in this range (eqn (3), V_0: zero-point volume).

$$V = V_0 \exp(\gamma T) \tag{3}$$

For **1a** ($V_0 = 2589(3)$ Å^3, $\gamma = 245(1) \times 10^{-6}$ K^{-1}), the results show a strong deviation from simple thermal expansion starting at about 225 K. In **1b** ($V_0 = 2993(3)$ Å^3, $\gamma = 227(5) \times 10^{-6}$ K^{-1}), a significant, but less pronounced aberration is found for the last data points (see Fig. 5). As these phenomena are due to a thermal spin-crossover (*vide infra*), a transition temperature $T_{1/2}$ well above 260 K—and thus extraordinarily high and near r.t.—may be assumed for [FeL(NCS)$_2$]·2CHCl$_3$ (**1b**). Because of the concomitant decomposition of crystals of **1b**, only data for **1a** could be further evaluated. For this purpose, the extrapolated (eqn (3)) cell volume, which accounts only for thermal expansion, was subtracted from the measured cell volume, leaving the volume increment V_{SCO} due to spin crossover. Rescaling to the maximum of 45(7) Å^3 provides γ_{HS} (see

§ Additionally, dark red columns of [FeL(NCS)$_2$]·CD$_2$Cl$_2$ were obtained by slow evaporation of a solution in [D$_2$]dichloromethane during one week. C$_{23}$H$_{22}$Cl$_2$D$_2$FeN$_6$S$_2$ (CCDC 960956), $M = 577.36$, monoclinic, $a = 9.1440(2)$, $b = 12.7087(4)$, $c = 22.2852(7)$ Å, $\beta = 107.386(3)°$, $V = 2471.41(12)$ Å^3, $T = 150.0(1)$ K, space group $P2_1/c$ (no. 14), $Z = 4$, 20 548 reflections measured, 4855 unique ($R_{int} = 0.0325$) which were used in all calculations. Final $R_1 = 0.0463$ and w$R_2 = 0.0875$ for all data (see Fig. S2†).
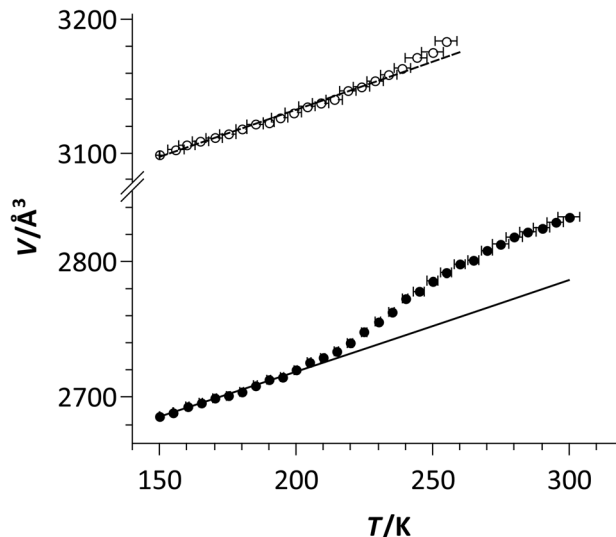
Fig. 5 Plot of the cell volume *vs.* temperature for **1a** (solid circles, solid line) and **1b** (hollow circles, dashed line) with partial fit based on the fundamental thermal-expansion model (eqn (3)).
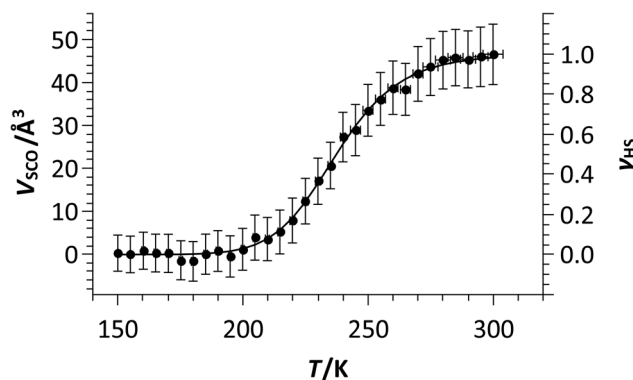

Fig. 6 Plot of the SCO volume increment and the molar HS fraction *vs.* the temperature for **1a** with fit based on the non-interaction model (eqn (2)).

Fig. 6). Again, these data, carrying the absolute error of the measured volume, may be fitted to the non-interaction model (eqn (2)).

The resulting parameters (see Table 6) show that the transition temperature $T_{1/2}$ falls into the same region as for solution and powder. The broadness ΔT_{80} is much less than in those cases, owing to a certain degree of intermolecular interactions in the crystal. Still, the value is quite large compared to other iron(II) complexes of this class; the transition remains gradual. The molar SCO enthalpy $\Delta_{SCO}H_m$ and entropy $\Delta_{SCO}S_m$ are about 1.5 times as high in the crystal. The former is due to a further stabilisation of the LS state compared to the HS state, through stronger intermolecular interactions. Similar to the compound [Fe^{II}(NCS)$_2$(phen)$_2$], a roughly equal distribution of the entropy gain between magnetic contribution, intramolecular stretching and deformation vibrations was found;[24] the larger SCO entropy may be attributed to the more efficient

coupling of molecular vibrations to lattice phonons. In the crystalline state—being the most highly ordered state of aggregation—the maximum possible interaction for any one substance is achieved. In our case, however, the simple non-interacting model is still valid to describe SCO behaviour. This is corroborated by the high coefficient of determination. This leads us to conclude a low overall degree of cooperativity.

Crystal structures

Molecular geometry. The crystal structures of **1a** and **1b** were determined at 150 K and 273 K (for details, see Table 1). In spite of the decomposition of crystals of **1b** above 255 K, a quick diffraction measurement was possible. Both pseudopolymorphs crystallise in the monoclinic space-group type $P2_1/c$ with one molecule per asymmetric unit. At r.t., they are optically discernible: while crystals of **1a** are orange (changing to dark red upon cooling, see Fig. S3†), those of **1b** are dark red. As the latter colour is associated with the LS state (*cf.* UV/Vis spectrometry in solution), **1a** seems to exist mainly in the high-spin, **1b** predominantly in the low-spin state under

ambient conditions. This supports the assumption of different SCO transition temperatures, the one of **1b** being significantly higher (and probably above r.t.).

In iron complexes, the coordinative bond lengths and the distortion of the coordination polyhedron are sensitive to the spin state of the central ion. To monitor the temperature-dependent changes, the Fe–N bond-lengths and their average $\bar{d}$ (Fe–N) were determined (see Table 2). Molecular distortion was evaluated using two established parameters: Σ is the sum of the deviation of all *cis*-angles θ_i from 90° in a distorted octahedron ($\Sigma = \sum_{i=1}^{12} |90° - \theta_i|$).[25] This parameter is readily obtainable, but invariant to changes in bond lengths. A more sophisticated approach is the application of continuous symmetry measures (CSM) that quantify "the minimal distance movement that the points of an object have to undergo in order to be transformed into a shape of the desired symmetry".[26] In our case, the reference shape was that of an ideal octahedron. The corresponding CSM is called $S(O_h)$ and—as a distance scaled to the size of the molecule—a dimensionless quantity.

Table 1 Crystallographic data and refinement details for solvates of **1**, **2** and **3**

	1·CHCl₃ (1a)		1·2CHCl₃ (1b)		2·CH₃OH	3
Temperature/K	150(1)	273(2)	150.0(2)	273.0(2)	150.0(1)	150.0(1)
CCDC no.	960951	960952	960953	960954	960955	960957
Sum formula	$C_{23}H_{23}Cl_3FeN_6S_2$		$C_{24}H_{24}Cl_6FeN_6S_2$		$C_{21}H_{26}Cl_2FeN_4O$	$C_{20}H_{22}Cl_2F_6FeN_4P$
M/g mol⁻¹	609.79		729.16		477.21	590.14
Crystal system	Monoclinic		Monoclinic		Monoclinic	Triclinic
Space group	$P2_1/c$ (no. 14)		$P2_1/c$ (no. 14)		$P2_1/c$ (no. 14)	$P\bar{1}$ (no. 2)
a/Å	18.1455(13)	18.242(8)	13.7750(18)	13.8495(12)	9.8322(7)	8.9533(5)
b/Å	9.2914(8)	9.322(3)	15.5077(14)	15.7047(11)	14.7903(7)	10.8208(7)
c/Å	16.4133(13)	16.786(7)	14.5434(19)	14.7310(14)	15.1031(12)	12.7219(7)
α/°	90	90	90	90	90	92.040(5)
β/°	104.815(7)	104.10(4)	91.427(13)	91.087(8)	93.936(8)	106.526(5)
γ/°	90	90	90	90	90	93.255(5)
V/Å³	2675.2(4)	2768.5(19)	3105.8(6)	3203.4(5)	2191.1(3)	1177.98(12)
Z	4	4	4	4	4	2
ρ_{calc}/g cm⁻³	1.514	1.463	1.559	1.512	1.447	1.664
Crystal description	Dark red plate	Orange plate	Dark red plate	Dark red prism	Light red prism	Pale orange prism
Crystal dimensions/mm³	0.15 × 0.13 × 0.03	0.18 × 0.13 × 0.04	0.15 × 0.08 × 0.07	0.30 × 0.14 × 0.07	0.17 × 0.14 × 0.10	0.17 × 0.13 × 0.07
μ/mm⁻¹	1.044	1.009	1.163	1.128	0.952	1.000
T(min, max)	0.86223/1.00000	0.75056/1.00000	0.54673/1.00000	0.88320/1.00000	0.29154/1.00000	0.78828/1.00000
θ(min, max)/°	3.35/26.00	3.31/26.00	3.24/26.00	3.30/25.00	3.29/26.00	3.35/26.00
Miller indices	$-22 \leq h \leq 22$, $-11 \leq k \leq 4$, $-20 \leq l \leq 12$	$-20 \leq h \leq 22$, $-10 \leq k \leq 11$, $-20 \leq l \leq 20$	$-16 \leq h \leq 16$, $-18 \leq k \leq 19$, $-16 \leq l \leq 17$	$-15 \leq h \leq 16$, $-18 \leq k \leq 13$, $-17 \leq l \leq 14$	$-10 \leq h \leq 12$, $-18 \leq k \leq 14$, $-11 \leq l \leq 18$	$-11 \leq h \leq 9$, $-13 \leq k \leq 12$, $-15 \leq l \leq 15$
Measured reflections	10 615	13 767	24 699	13 334	9403	9564
Independent reflections (R_{int})	5248 (0.0786)	5436 (0.0952)	6079 (0.0676)	5553 (0.0767)	4295 (0.0280)	4620 (0.0259)
Observed reflectionsᵃ (R_σ)	3319 (0.1276)	3116 (0.1245)	4964 (0.0539)	3285 (0.1150)	3400 (0.0389)	4042 (0.0390)
Data, restraints, parameters	5248/66/356	5436/54/347	6079/66/392	5553/66/392	4295/0/267	4620/135/365
R_1/wR_2ᵇ (all data)	0.1293/0.1364	0.1553/0.2009	0.0724/0.1336	0.1490/0.1686	0.0488/0.0975	0.0454/0.0950
R_1/wR_2ᵇ (observed data)ᵃ	0.0748/0.1146	0.0842/0.1615	0.0559/0.1247	0.0824/0.1402	0.0372/0.0949	0.0376/0.0908
u, vᵇ	0.0273/0.0000	0.0602/1.9445	0.0555/3.6304	0.0442/1.9887	0.0552/0.0000	0.0472/0.4573
S, S'	1.054/1.090	1.052/1.098	1.067/1.075	1.090/1.097	1.086/1.086	1.064/1.088
ρ_e (min, max)/e Å⁻³	−0.477/0.509	−0.506/0.506	−0.560/0.672	−0.352/0.432	−0.740/0.996	−0.294/0.367

ᵃ $I > 2\sigma(I)$. ᵇ $R_1 = \sum ||F_o| - |F_c||/\sum |F_o|$, w$R_2 = [\sum w(F_o^2 - F_c^2)^2/\sum wF_o^4]^{1/2}$, w $= [\sigma^2(F_o^2) + (uP)^2 + vP]^{-1}$ with $P = [\max(F_o^2, 0) + 2F_c^2]/3$.

Table 2 Fe–N bond lengths and distortion parameters of **1a** and **1b**

	[FeL(NCS)$_2$]·CHCl$_3$ (**1a**)		[FeL(NCS)$_2$]·2CHCl$_3$ (**1b**)	
T/K	150	273	150	273
Assigned state	LS-Fe^{II}	HS-Fe^{II}	LS-Fe^{II}	LS/HS-Fe^{II}
d(Fe1–N10)/Å	1.918(4)	2.101(5)	1.923(3)	2.013(4)
d(Fe1–N20)/Å	1.978(4)	2.117(5)	1.970(3)	2.041(5)
d(Fe1–N30)/Å	1.959(4)	2.183(5)	1.970(3)	2.057(5)
d(Fe1–N41)/Å	2.114(4)	2.252(5)	2.119(3)	2.179(6)
d(Fe1–N50)/Å	1.972(4)	2.032(6)	1.957(3)	1.994(6)
d(Fe1–N60)/Å	1.988(4)	2.099(6)	1.992(3)	2.050(6)
$\bar{d}$(Fe–N)/Å	1.99(3)	2.13(3)	1.99(3)	2.06(3)
Σ/°^{a}	48.3(7)	85.2(7)	52.1(5)	66.8(7)
$S(O_h)^a$	0.69	1.52	0.76	1.09

^{a} See text for the definition of symmetry parameters.

Fig. 7 ORTEP plot of **1a** at 150 K (left) and 273 K (right). Ellipsoids of 50% probability; hydrogen atoms and solvent molecule at high temperature omitted for clarity.

For comparison and assignment of predominant spin states, complexes with weak-field chlorido ligands in the oxidation states +II (**2**) and +III (**3**) were also analysed by X-ray diffractometry (for molecular graphics, see Fig. S4†). Data for the LS complex [Fe(CN)$_2$L] carrying two strong-field cyanido ligands have been published before (see Table 3).[18]

At 150 K, as is evident from the data in Table 2, both pseudopolymorphs (**1a**, **1b**) are characterised by parameters that are typical for LS-iron(II) complexes with nitrogen donors: an average Fe–N bond length of about 2.0 Å and a weakly distorted coordination pseudo-octahedron ($\Sigma \approx 50°$, $S[O_h] < 1$). Thus, it is justified to assign the structures a pure low-spin state (in accordance with the data of the dicyanido complex, Table 3).

When heated to 273 K, [FeL(NCS)$_2$]·CHCl$_3$ (**1a**) adopts a structure close to one characteristic of HS-iron(II) complexes (see Fig. 7): the average bond length rises by $\Delta \bar{d}$ (Fe–N) = 0.14 Å (to a value near the expected *ca.* 2.2 Å), the angular distortion by $\Delta\Sigma = 36.9°$ and the CSM by $\Delta S(O_h) = 0.83$.

The deviations from the values obtained for the HS-model **2**·CH$_3$OH, which are even greater, are due to the different character of the anionic ligands (chlorido *vs.* thiocyanato-κ*N*):

Table 3 Coordinative bond lengths and distortion parameters for spin-state model-complexes at 150 K

	[Fe(CN)$_2$L]·2CH$_3$OH^a	[FeCl$_2$L]·CH$_3$OH (**2**·CH$_3$OH)^b	[FeCl$_2$L]PF$_6$ (**3**)^b
μ_{eff}^{c}	0.83(4)	5.0(2)	5.75(4)
State	LS-Fe^{II}	HS-Fe^{II}	HS-Fe^{III}
d(Fe1–N10)/Å	1.938(2)	2.170(2)	2.124(2)
d(Fe1–N20)/Å	1.965(2)	2.194(2)	2.145(2)
d(Fe1–N30)/Å	1.993(2)	2.225(2)	2.196(2)
d(Fe1–N41)/Å	2.111(2)	2.291(2)	2.215(2)
d(Fe1–X1)/Å^d	1.923(2)	2.3455(7)	2.2250(7)
d(Fe1–X2)/Å^d	1.929(3)	2.5569(8)	2.3187(7)
$\bar{d}$(Fe–N)/Å	2.00(4)	2.22(3)	2.17(3)
Σ/°^{e}	48.5(3)	98.8(3)	84.5(3)
$S(O_h)^e$	0.66	2.47	1.66

^{a} Structure published elsewhere.[18] ^{b} See Fig. S4. ^{c} Effective magnetic moment of powders at r.t. as determined by susceptometry. ^{d} X1: donor atom *trans* to N10, X2: donor atom *trans* to N30. ^{e} See text for the definition of symmetry parameters.
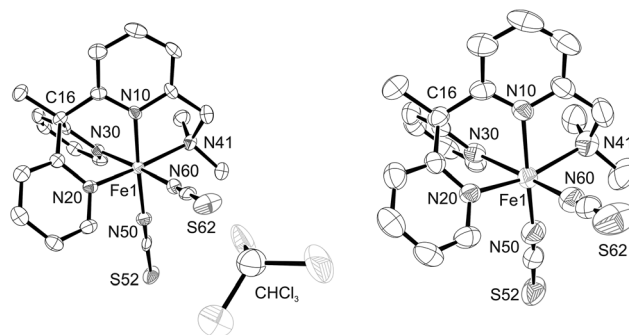
while Fe–Cl bonds are considerably longer than Fe–N bonds (thus increasing the CSM), the weaker π bonding in **2** causes the *cis*-angles to be more irregular (thereby increasing Σ). Comparing the data with those of other bis(thiocyanato-κ*N*)iron(II) complexes and taking into account the spin-transition curve (see Fig. 6), it is reasonable to assume a virtually complete SCO for **1a** at 273 K.[23,27] The notable changes in molecular geometry are illustrated by an overlay of the complexes at both temperatures (see Fig. 8). The rigidity of the substituted tris-(pyridyl)ethane ligand-"cap" imposes another remarkable feature: because of the coordinative bond elongation attendant on spin-crossover, the non-bonding distance between the iron(II) ion Fe1 and the quaternary carbon atom C16 increases from 3.050(5) Å at 150 K to 3.243(5) Å at 273 K.

The findings of **1a** are in contrast to those of [FeL(NCS)$_2$]·2CHCl$_3$ (**1b**). In accordance with cell-volume behaviour (see Fig. 5), a late-onset SCO is found. At 273 K, the observed structural parameters are significantly above the estimates for a pure LS state, but far too low for a pure HS state (see Fig. 9). The non-bonding distance between Fe1 and C16 increases only from 3.063(6) Å to 3.147(6) Å. A rapid diffraction experiment at 300 K, while suffering from severe degradation of the crystal, hinted towards further progression to a proper HS structure. Therefore, we conclude that **1b** is capable of a high-
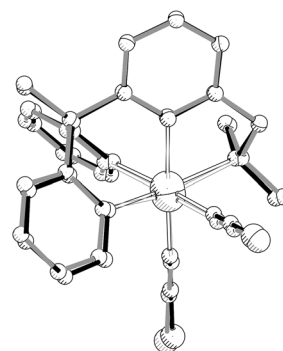

Fig. 8 PLATON/PLUTON plot showing the superposition of HS-**1a** (273 K, grey) and LS-**1a** (150 K, black). Atoms with arbitrary radii; hydrogen atoms and solvent molecules omitted for clarity.
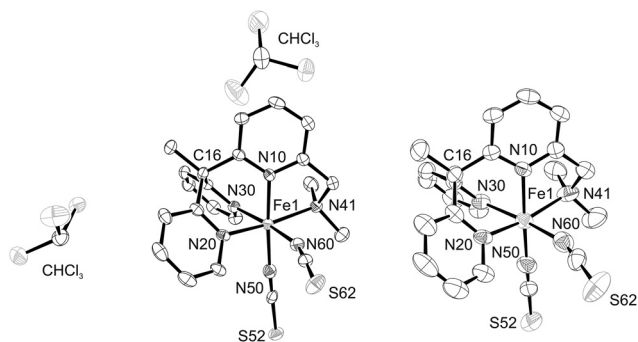
Fig. 9 ORTEP plot of **1b** at 150 K (left) and 273 K (right). Ellipsoids of 50% probability; hydrogen atoms and solvent molecules at high temperature omitted for clarity.

temperature thermal spin crossover which, however, is obscured by the deterioration of the crystal.

Intermolecular interactions

In crystals of **1b**, infinite chains of complexes along [100] are formed by one π stack and two edge-on contacts per adjacent molecule (see Fig. S5†). At 150 K, each thiocyanato ligand exhibits three intermolecular contacts: one NCS ligand has two aromatic interactions with a neighbouring complex (d[C13···C61] = 3.440[6] Å, d[C14···C61] = 3.495[6] Å) and a CH-S contact with a chloroform molecule (d[C1···S62] = 3.812[6] Å). The other ligand has a CH–S contact with a complex (d[C34···S52] = 3.655[4] Å), is close to a chloroform molecule (d[C5A···S52] = 3.566[9] Å), and has a Cl–S contact with another solvent molecule (d[S52···Cl6A] = 3.380[5] Å). At 273 K, these distances are the same within the limits of uncertainty, suggesting effects of ordinary thermal expansion—not an SCO.

In contrast, the crystal structure of **1a** is characterised by dimeric clusters, in which the molecules hold together *via* one π stack (formed by the rings R2x containing N20, see Fig. S6†) and two edge-on contacts to an adjacent pyridyl residue (R3x containing N30). Additionally, a CH–S contact between a pyridyl residue and a thiocyanato ligand (C24···S52) is found. The dimers are connected to zigzag chains propagating along [001] by two contacts per neighbour—between the second thiocyanato ligand and the adjacent pyridinediyl residue (S62···C14) or the adjacent carbon-bound methyl group (C61···C17), respectively (see Fig. S7†). The chloroform molecules constitute layers in (100) and interact with the complexes *via* a CH–S (C1A···S62), a halogen–aryl (Cl3A···C13) and a halogen–methylene contact (Cl2A···C40). Compared to the structure at 150 K, only the CH–S contacts between and within dimers are significantly lengthened at 273 K (see Table 4). This reflects weaker intermolecular contacts in the HS state, thus leading to a higher SCO enthalpy than in solution or the powder. The π-stacking distance, on the other hand, is significantly shorter. By comparison with the findings in **1b**, these changes must be caused by a spin-state transition, as opposed to the small effects of thermal expansion.

Table 4 Intermolecular contacts and associated distances for **1a**

T/K	150	273	Difference
d(R2x···R2x)/Å[a]	3.795(8)	3.727(8)	−0.07(2)
d(C24···S52)/Å	3.672(5)	3.767(7)	0.095(9)
d(S62···C14)/Å	3.715(6)	3.757(9)	0.04(1)
d(C61···C17)/Å	3.580(8)	3.59(1)	0.01(2)
d(C1A···S62)/Å	3.65(2)	3.68(2)	0.03(3)
d(Cl3A···C13)/Å	3.42(1)	3.44(1)	0.02(2)
d(Cl2A···C40)/Å	3.56(1)	3.58(1)	0.02(2)

[a] Distance of ring centroids.

In both pseudopolymorphs, a three-dimensional network is formed by interactions *via* thiocyanato ligands and involving solvent molecules. The formation of complex dimers in **1a** and infinite complex chains in **1b** is presumably the main reason for their differing SCO properties. In **1a**, the transition to the HS state leads to a shortening of aromatic contacts. Such a compression is energetically less favoured in **1b**, where twice as many interactions per complex molecule and long-range ordering *via* aromatic contacts are present. This may result in a considerably larger SCO enthalpy and thus a higher transition temperature. The strengths and lengths of CH–S contacts (also involving solvent molecules) play a major role in the degree of cooperativity in a crystal. These parameters thereby affect the abruptness of an SCO as well as the broadness of a hysteresis, if present.[23] As the pseudopolymorphs of [FeL(NCS)₂] (**1**) also differ with respect to such interactions, the transitions are expected to show different characteristics.

Evaluation of the thermal-expansion tensor

In contrast to the microscopic views of molecular structure and intermolecular forces, the evaluation of temperature-dependent expansion of the crystal itself offers a connection between the molecular level and the macroscopic world of materials. Therefore, we calculated the thermal-expansion tensor $\boldsymbol{\alpha}$ from the cell constants at different temperatures. Following Neumann's principle, it takes the form of a symmetric 3 × 3 matrix with four non-zero components (see eqn (4)) for monoclinic crystals.

$$\boldsymbol{\alpha} = \begin{pmatrix} \alpha_{11} & 0 & \alpha_{13} \\ 0 & \alpha_{22} & 0 \\ \alpha_{13} & 0 & \alpha_{33} \end{pmatrix} \qquad (4)$$

The basis of this second-order tensor is a Cartesian coordinate system with x, y and z as main axes of expansion. Its trace is the volumetric expansion coefficient γ. For the standard setting, the y axis coincides with the crystallographic b axis, thus $\alpha_{22} = \alpha_b$. The other components in the crystallographic coordinate system are obtained by a rotation of the remaining axes in the xz plane (angles μ_{1a} between x and a, μ_{3c} between z and c). In order to calculate α, the evolution of the cell constants with temperature has to be fitted with analytical functions (see Fig. S8–S13 and Tables S1–S3†). In **1a**, the range between 150 and 200 K is dominated by thermal expansion and has therefore been selected for the first fit. Representative

Table 5 Diagonal elements α_{ii} of the Cartesian expansion tensor, coefficients α_x of thermal expansion along the cell metrics, volumetric expansion coefficient γ and angles μ_{ix} between Cartesian and crystallographic axes in the xz plane for **1a** and **1b**

	1a			1b
T/K	175	238	Difference	175
Fit interval/K	[150, 200]	[220, 280]		[150, 240]
Regime	Thermal	Thermal, SCO	SCO	Thermal
$\alpha_{11}/10^{-6}$ K^{-1}	32.3	147		29.4
$\alpha_{22}/10^{-6}$ K^{-1}	81.8	54.2		72.4
$\alpha_{33}/10^{-6}$ K^{-1}	135	338		126
$\mu_{1a}/°$	13.6	15.5		19.1
$\mu_{3c}/°$	28.4	30.0		20.6
$\alpha_a/10^{-6}$ K^{-1}	55.5	195	140	41.3
$\alpha_b/10^{-6}$ K^{-1}	81.8	54.2	−27.6	72.4
$\alpha_c/10^{-6}$ K^{-1}	111	290	179	114
$\alpha_\beta/10^{-6}$ K^{-1}	−42.8	−82.5	−39.7	−31.7
$\gamma/10^{-6}$ K^{-1}	249	539	290	227

Table 6 Thermodynamic and statistical parameters for the SCO of [FeL(NCS)$_2$] (**1**) in different states of aggregation

	Solution (acetone)	Powder (**1**)[a]	Crystal (**1a**)	Surface (HOPG)[a]
$T_{1/2}$/K	234(3)	251(3)	240(3)	235(6)
ΔT_{80}/K	58(4)	62(4)	35(4)	115(8)
$\Delta_{SCO}H_m$/kJ mol^{-1}	22.5(6)	22.8(5)	36.9(10)	10.0(10)
$\Delta_{SCO}S_m$/J K^{-1} mol^{-1}	96(3)	92(2)	155(5)	45(5)
R^2	0.9997	0.9983	0.9941	0.9710
$\bar{R}^2$	0.9996	0.9982	0.9933	0.9657

[a] Data have been published before and are included for comparison.[17]

data are given for 175 K, the centre of the interval (see Table 5). The slight difference in the volumetric expansion coefficient γ compared to the value from above is due to an exponential function being used here instead of a polynomial. In the range between 220 and 280 K, the SCO effects are superimposed. As they are maximal at $T_{1/2}$, α is given for 238 K. The difference of the tensors at both temperatures may be used as a rough estimate of SCO-only effects. (Because the bases are rotated with respect to one another—as shown by different μ_{1a} and μ_{3c}—the differences of the Cartesian tensor components

α_{ii} have no meaningful spatial correlate.) For **1b**, the regime of thermal expansion is much greater, allowing for evaluation of the range between 150 and 240 K. The specification of the tensor at 175 K was chosen for reasons of comparability. In addition, Fig. 10 represents the thermal-expansion tensor as a three-dimensional isosurface, also indicating the position of the Cartesian and crystallographic axes.

At 175 K, both tensors show similar features that of **1b** being slightly smaller in all components. (This may be due to the incorporation of more solvent, which interacts only weakly *via* compressible contacts leading to a less rigid structure.) The main component of the expansion falls upon the b and c axes, while it is less pronounced in the direction of a. In **1b**, a points along the chains of complexes connected by π stacks and edge-on contacts. In **1a**, this is the direction of the corresponding interactions within the dimers.

Along c, no strong contacts are found. Thus, crystals of the pseudopolymorphs of [FeL(NCS)$_2$] (**1**) preferentially expand in directions without strong (aromatic) dispersion forces as this requires less energy.

During spin crossover in **1a**, the expansion coefficient at 238 K along a (c) is more than 3.5 (2.5) times as large as in the purely thermal regime (175 K). Surprisingly, along b, it is smaller at 238 K than at 175 K. The CH–S contacts between complexes, in contrast to those between complex and solvent molecules, run along [101].

Owing to Fe–N bond dilatation with no simultaneous change in Fe–NCS angle, the a and c vectors are stretched particularly strongly. In addition, the rigid substituted tris(pyridyl)ethane "caps" coordinate along c and are "pushed away" during SCO (*vide supra*). The gradual contraction of π stacks (see Table 4) leads to the decrease in expansion along b.

Comparison to behaviour on the HOPG surface

In solution, spin crossover progresses without any interaction between complex molecules. In the crystal, one finds the strongest possible interactions for a particular compound because of the long-range 3D order.

On a non-interacting surface, one would expect an intermediate behaviour due to (at least partial) 2D order. However,
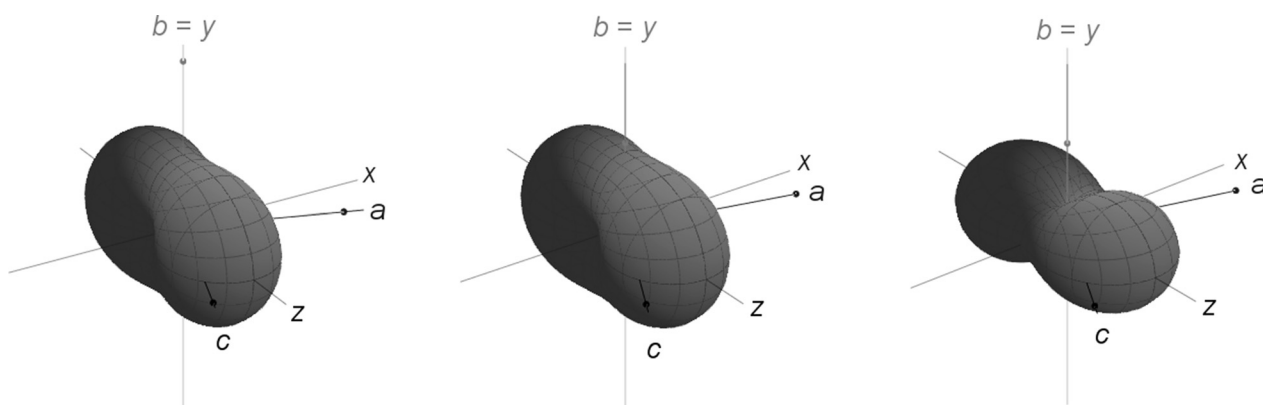

Fig. 10 Visualisation of the expansion tensors of **1b** at 175 K (left), of **1a** at 175 K (middle) and at 238 K (right).

for [FeL(NCS)$_2$] (**1**) on HOPG, we found a significantly altered SCO. With ΔT_{80} = 115(8) K, the transition is extremely broad, even broader than in solution. As the width usually correlates with the strength of interaction (weaker interaction resulting in broader transitions), less interaction cannot be the explanation for the even broader transition on HOPG. We therefore conclude that this effect is due to a complex–substrate interaction of a kind yet to be determined.

On the surface, the molar SCO enthalpy and entropy are less than half as large as in solution, which means that the LS state is enthalpically and the HS state entropically less favoured.[17] A possible explanation is the formation of a two-dimensional HS lattice on HOPG through high-temperature vapour deposition. When cooling the sample, interactions with the surface do not allow for relaxation into the energetically most preferable LS arrangement, thereby lessening $\Delta_{SCO}H_m$. As this non-optimal lattice has a lower degree of order, $\Delta_{SCO}S_m$, which signifies the difference in the "orderedness" of both states, is also decreased.

The lower coefficient of determination shows the fit to be less adequate to describe the behaviour on the surface. The non-interaction model (HS-**1** ⇌ LS-**1**) presumably fails because of specific interactions with the substrate.

Experimental

Materials and analytical methods

Reagents were purchased from Acros Organics or Sigma-Aldrich and used without further purification. Solvents were purified according to standard procedures.[28] The ligand L was synthesised following literature instructions.[18,29]

NMR spectra were recorded on a "Bruker ARX 200" at r.t. Chemical shifts refer to SiMe$_4$, CCl$_3$F and H$_3$PO$_4$ (85% in H$_2$O) for ^{1}H, ^{19}F and ^{31}P, respectively. They have been calibrated with respect to the residual proton signal for ^{1}H ((D$_5$)DMSO: δ = 2.50 ppm, CD$_2$HOD: δ = 3.31 ppm)[30] or an electronically stored frequency for the other nuclei.

IR spectra in attenuated total reflectance (ATR) were measured with a "Thermo Nicolet iS5" equipped with a "Thermo Nicolet iD5" ZnSe sample-holder, those of CsCl pellets with a "Nicolet Magna System 750".

Mass spectra were recorded in ESI(+) mode with a "Thermo Scientific Orbitrap LTQ XL" (spray voltage: 5 kV, source temperature: 275 °C).

UV/Vis spectra were obtained using a "Varian Cary 50" spectrophotometer.

Elemental analyses were performed using "Thermo Finnigan EAGER 300" and "elementar vario EL" devices.

Susceptometry was carried out at r.t. using a "Johnson Matthey MSB Auto" magnetic balance calibrated with tridistilled water (χ_g = −7.2 × 10^{-7} cm^3 g^{-1}). The susceptibility of L measured in MeOH was χ_D = −2.07 × 10^{-4} cm^3 mol^{-1}; further diamagnetic contributions were corrected for using Pascal's constants.[31]

Synthesis of [FeL(NCS)$_2$] (1). In addition to the route starting from [Fe(NCS)$_2$(py)$_4$] (py: pyridine),[17] [FeL(NCS)$_2$] (**1**) may be prepared conveniently from iron(II) chloride in a two-step one-pot reaction.

To a colourless solution of L (304 mg, 0.955 mmol) in MeOH (30 mL), FeCl$_2$ (109 mg, 0.860 mmol) was added while stirring at r.t. After 45 min, (nBu$_4$N)SCN (778 mg, 2.59 mmol) in MeOH (10 mL) was added to the brownish-yellow solution. The resulting brown suspension was stirred for two days and filtered. The deep-brown residue was successively washed with water, MeOH and Et$_2$O (2 × 5 mL each). Evaporation of solvent residues in medium vacuum yielded **1**·H$_2$O (330 mg, 75%) as a brown powder.

Solvent-free [FeL(NCS)$_2$] was obtained upon recrystallisation from CHCl$_3$–Et$_2$O (see below), grinding the polycrystalline material in a mortar and drying it in medium vacuum at 60 °C. The two pseudopolymorphs [FeL(NCS)$_2$]·CHCl$_3$ (**1a**) and [FeL(NCS)$_2$]·2CHCl$_3$ (**1b**) co-crystallised from chloroform solutions upon vapour diffusion of diethyl ether at r.t. for three days.§

^{1}H NMR (200 MHz, (D$_6$)DMSO): δ 130.3, 77.3, 74.3, 65.4, 54.5, 44.9, 37.1, 35.3, 20.8, −2.9 ppm (all br s). UV/Vis (MeOH): λ_{max} (ε) 416 (1100), 262 (13 100), 209 nm (32 200 cm^2 mmol^{-1}). IR spectrum, ESI(+) mass-spectrum and elemental analysis comply with previously published data.[17]

Synthesis of [FeCl$_2$L] (2). To a colourless solution of L (140 mg, 0.440 mmol) in MeOH (1.5 mL), FeCl$_2$·4H$_2$O (80 mg, 0.40 mmol) in MeOH (1.5 mL) was added dropwise while stirring at r.t. The brownish-yellow solution was stirred for a further 30 min. Afterwards, the resulting complex was precipitated exhaustively with MTBE. The powder was filtered off and washed with MTBE (3 × 30 mL). Evaporation of solvent residues in medium vacuum for 12 h yielded **2**·2H$_2$O (157 mg, 82%) as an orange-brown powder.

Crystals fit for X-ray diffractometry formed by precipitation upon vapour diffusion of diethyl ether into methanolic solutions of the complex at r.t. for two weeks.

^{1}H NMR (200 MHz, CD$_3$OD): δ 92.5, 77.8, 76.5, 71.5, 61.7, 53.4, 42.8, 38.6, 32.9, 17.1 (all br s), 15.3–12.4 (br m), 0.85 ppm (s). IR (CsCl): $\tilde{\nu}$ 3070, 2997, 2984, 2965, 2888 (m, ν[CH]), 1593, 1578 (vs, ν[C=N], ν[C=C]), 1476, 1436, 1383 (vs, δ[CH]), 1309 (w), 1295, 1252, 798, 770, 757, 748 (m, γ[CH]), 628 (m, δ[C=C], δ[C=N]), 427 (m, γ[C=C], γ[C=N]), 255 cm^{-1} (m, ν[FeCl]). ESI(+) MS (MeOH): m/z (%) 409.09 (100, [M − Cl]$^+$), 319.19 (55, [L + H]$^+$). UV/Vis (MeOH): λ_{max} (ε) 353 (1900), 263 (13 900), 206 nm (26 700 cm^2 mmol^{-1}). Anal. calcd for C$_{20}$H$_{26}$Cl$_2$FeN$_4$O$_2$ (481.20): C 49.92, H 5.45, N 11.64%; found C 49.93, H 5.15, N 11.44%.

Synthesis of [FeCl$_2$L]PF$_6$ (3). To a colourless solution of L (227 mg, 0.713 mmol) in MeOH (10 mL), FeCl$_3$·6H$_2$O (175 mg, 0.647 mmol) was added while stirring at r.t. From the yellow-brown solution, an orange-yellow powder precipitated promptly. To the resulting suspension, (nBu$_4$N)PF$_6$ (251 mg, 0.648 mmol) was added. Using airflow, the mixture was briefly heated to boiling to dissolve the precipitate. During 1.5 h of stirring at r.t., a bright yellow suspension formed that was held at −20 °C for another 1.5 h. The mixture was filtered and the microcrystalline solid washed with MeOH and MTBE (2 × 2.5 mL each). The resulting powder was recrystallised from

MeCN (5 mL) by vapour diffusion of Et$_2$O at r.t. During eleven days, large cuboid orange-yellow crystals formed which were suitable for X-ray diffractometry. After selection of single crystals, the remaining solid was filtered off, washed with Et$_2$O (3 × 10 mL) and pulverised. Evaporation of solvent residues in medium vacuum yielded **2** (304 mg, 80%) as a yellow powder.

^{1}H NMR (200 MHz, (D$_6$)DMSO): δ 8.42 (br m, 2H, 6′-H, 6″-H), 7.62 (br m, 3H, 4-H, 4′-H, 4″-H), 7.25–7.16 (br m, 3H, 3-H, 3′-H, 3″-H), 6.97 (br m, 3H, 5-H, 5′-H, 5″-H), 4.29 (br s, 2H, CH$_2$), 2.63 (br s, 6H, N–CH$_3$), 2.16 ppm (br s, 3H, C–CH$_3$).¶ ^{19}F NMR (188 MHz, (D$_6$)DMSO): δ −70.0 ppm (d, $^1J_{FP}$ = 710 Hz, PF$_6^-$). ^{31}P NMR (81 MHz, (D$_6$)DMSO): δ −144.2 ppm (sept, $^1J_{PF}$ = 710 Hz, PF$_6^-$). IR (ATR): $\tilde{\nu}$ 3123, 2988, 2903, 2813 (w, ν[CH]), 1594, 1579 (m, ν[C=N], ν[C=C]), 1478, 1464, 1444, 1436, 1397 (m, δ[CH]), 1309, 1298, 1282, 1239, 1203 (w), 1168, 1056, 1025, 1015, 1000, 972 (m), 833 (vs, ν[PF$_6$]), 788, 765, 758, 740, 710 (m, γ[CH]), 644, 638, 630 (m, δ[C=C], δ[C=N]), 599 cm^{-1} (s, δ[PF$_6$]). ESI(+) MS (MeOH): m/z (%) 444.06 (72, [M]$^+$), 440.11 (100, [M − Cl + OMe]$^+$), 409.09 (7, [M − Cl]$^+$), 319.19 (57, [L + H]$^+$). UV/Vis (MeOH): λ_{max} (ε) 354 nm (3200 cm^2 mmol^{-1}). Anal. calcd for C$_{20}$H$_{22}$Cl$_2$F$_6$FeN$_4$P (590.13): C 40.71, H 3.76, N 9.49%; found C 40.98, H 3.90, N 9.48%.

X-ray crystallography

Data were collected using an "Oxford Diffraction Xcalibur S" diffractometer equipped with a goniometer in κ geometry, a "Sapphire 3" CCD-detector, and a graphite-monochromated "Enhance" Mo-K$_\alpha$ source (λ = 0.71073 Å). Diffraction images were integrated with CrysAlisPro. An empirical absorption correction using spherical harmonics implemented in the SCALE3 ABSPACK scaling algorithm was performed.[32]

Structures were solved with SHELXS-97 using direct methods and refined with SHELXL-97 against F_o^2 data using the full-matrix least-squares algorithm.[33] Non-hydrogen atoms were refined anisotropically; hydrogen atoms were refined isotropically with standard riding-models.

The chloroform molecule in **1a**, one of two in **1b**, and the hexafluorophosphate ion in **3** exhibit rotational disorder. They have each been modelled in two discrete positions using same-distance, same-angle, tight rigid-bond and isotropy restraints for the halogen atoms. Partial occupations for the two orientations refined to *ca.* 0.5/0.5 in **1a** as well as in **3**, to *ca.* 0.67/0.33 in **1b** at 150 K and *ca.* 0.46/0.54 at 273 K.

Molecular graphics were produced using ORTEP-3 for Windows[34] and Mercury[35]. Molecular superpositions were performed using MOLFIT as implemented in the package WinGX[36] and visualised using PLATON/PLUTON.[37]

Temperature-dependent measurements of unit-cell parameters were conducted using an "Oxford CryojetXL" nitrogen gas-blower to raise the temperature from 150 K in steps of 5 K. At each temperature point, diffraction patterns were measured with an optimised time-constrained strategy (20 min, ω scans, $\theta_{max} \approx$

29°, *ca.* 44% completeness). Reflections were used only to determine unit-cell parameters without integration of the images.

Thermal-expansion tensors, their visualisations and derived quantities were calculated using a beta version of X-Ray TTT.[38] Continuous symmetry measures (CSM) were calculated using the internet service of the Hebrew University of Jerusalem.[39] All other parameters were derived from SHELXL-97 output using basic arithmetic or statistical methods.

Conclusions

[FeL(NCS)$_2$] (**1**) is capable of a complete, gradual, one-step thermal spin-crossover without hysteresis in solution and in crystals of the adduct **1**·CHCl$_3$ (**1a**). The features of the SCO are within the limits of other well-established examples of bis (thiocyanato-κN)iron(II) complexes. However, the transition temperature $T_{1/2}$ is quite high for the substance class and even higher in the case of crystalline **1**·2CHCl$_3$ (**1b**), showing a strong influence of the solvent in the solid state. Unfortunately, crystals of **1b** proved to be unstable at elevated temperature. A large $T_{1/2}$ is desirable for applications in data storage, making synthetic optimisation of the crystalline system **1**·x solvent a promising research goal.

The macroscopic crystal expansion due to spin-crossover correlates directly with molecular and intermolecular features. It occurs along the coordinates of molecular bond dilatation as predetermined by the denticity and rigidity of the ligands.

The different, yet still extant, SCO behaviour in direct contact with an HOPG surface seems to be based on interactions of the complex molecules with the substrate; no hints at intermolecular interactions were found. As is typical for (partly) aromatic compounds on graphite, **1** is probably interacting *via* its heteroaryl residues. Sterical hindrance does not allow for π stacking between complexes and surface apart from steep steps or ridges on the latter. However, since high surface coverage was achieved, and the number of steps or ridges should be limited on highly-oriented graphite, the adsorption *via* one or two edge-on contacts can be assumed. The rings containing N30 and N10 are particularly fit for this purpose, because adsorption would make the bulky thiocyanato ligands point away from the surface (see Fig. 11). Binding through the
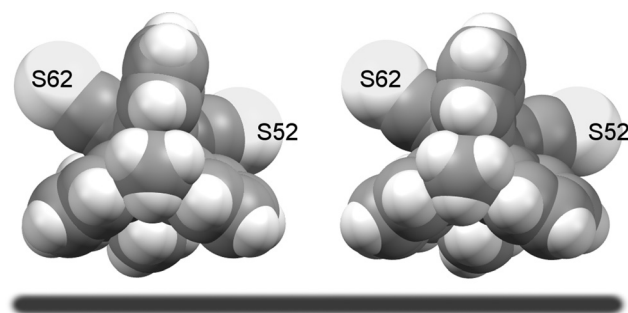

Fig. 11 Proposed adsorption mode of **1** on HOPG (dark grey line) as derived from the structure of **1a** at 150 K (left, low-spin) and 273 K (right, high-spin).

¶The numbering scheme is given in Fig. 2. Single and double primed numbers refer to—through coordination—chemically inequivalent pyridyl residues in an arbitrary fashion.

sulphur atoms of these—as often seen on metal surfaces—is improbable: no π···SCN contacts are found in the crystal structure of any pseudopolymorph.

As shown in Fig. 11, the tentative adsorption site of **1** changes little with temperature. Thus, a strong temperature dependence of the respective interactions is not expected. The main changes during SCO, as found by analysis of the thermal-expansion tensor, progress perpendicular to the viewing plane and *via* the sulphur atom(s) S52 (and S62). The assumption of an optimal two-dimensional HS lattice being disturbed by cooling and subsequent transition into a less than optimally packed LS state (*vide supra*) adequately explains the deviation from simple non-interaction models. The assumptions made can further be substantiated by determination of the exact topography of a submonolayer of **1** on HOPG. Work to this end is in progress.

Acknowledgements

Notes and references

1 A. D. McNaught and A. Wilkinson, *IUPAC. Compendium of Chemical Terminology*, Blackwell Scientific Publications, Oxford, 2nd edn, 1997.

2 Y. Garcia and P. Gütlich, in *Spin Crossover in Transition Metal Compounds II*, ed. P. Gütlich and H. A. Goodwin, Springer, Berlin, 2004, pp. 49–62.

3 J.-F. Létard, P. Guionneau and L. Goux-Capes, in *Spin Crossover in Transition Metal Compounds III*, ed. P. Gütlich and H. A. Goodwin, Springer, Berlin, 2004, pp. 221–249.

4 P. Gamez, J. S. Costa, M. Quesada and G. Aromí, *Dalton Trans.*, 2009, 7845–7853.

5 *Spin-Crossover Materials: Properties and Applications*, ed. M. A. Halcrow, John Wiley & Sons Ltd., 2013.

6 M. Tafili-Kryeziu, M. Weil, T. Muranaka, A. Bousseksou, M. Hasegawa, A. Jun and W. Linert, *Dalton Trans.*, 2013, **42**, 15796–15804.

7 S. Brooker and J. A. Kitchen, *Dalton Trans.*, 2009, 7331–7340.

8 K. P. Kepp, *Coord. Chem. Rev.*, 2013, **257**, 196–209.

9 N. Ballav, C. Wäckerlin, D. Siewert, P. M. Oppeneer and T. A. Jung, *J. Phys. Chem. Lett.*, 2013, **4**, 2303–2311.

10 H. J. Shepherd, G. Molnár, W. Nicolazzi, L. Salmon and A. Bousseksou, *Eur. J. Inorg. Chem.*, 2013, 653–661.

11 T. G. Gopakumar, F. Matino, H. Naggert, A. Bannwarth, F. Tuczek and R. Berndt, *Angew. Chem., Int. Ed.*, 2012, **51**, 6262–6266.

12 T. Miyamachi, M. Gruber, V. Davesne, M. Bowen, S. Boukari, L. Joly, F. Scheurer, G. Rogez, T. K. Yamada, P. Ohresser, E. Beaurepaire and W. Wulfhekel, *Nat. Commun.*, 2012, **3**, 938.

13 M. S. Alam, M. Stocker, K. Gieb, P. Müller, M. Haryono, K. Student and A. Grohmann, *Angew. Chem., Int. Ed.*, 2010, **49**, 1159–1163.

14 A. Grohmann, M. Haryono, K. Student, P. Müller and M. Stocker, *Eur. J. Inorg. Chem.*, 2013, 662–669.

15 P. Chakraborty, M.-L. Boillot, A. Tissot and A. Hauser, *Angew. Chem., Int. Ed.*, 2013, **52**, 7139–7142.

16 B. Warner, J. C. Oberg, T. G. Gill, F. El Hallak, C. F. Hirjibehedin, M. Serri, S. Heutz, M.-A. Arrio, P. Sainctavit, M. Mannini, G. Poneti, R. Sessoli and P. Rosa, *J. Phys. Chem. Lett.*, 2013, **4**, 1546–1552.

17 M. Bernien, D. Wiedemann, C. F. Hermanns, A. Krüger, D. Rolf, W. Kroener, P. Müller, A. Grohmann and W. Kuch, *J. Phys. Chem. Lett.*, 2012, **3**, 3431–3434.

18 D. Wiedemann, E. Świętek, W. Macyk and A. Grohmann, *Z. Anorg. Allg. Chem.*, 2013, **649**, 1483–1490.

19 F. Felix, J. Ferguson, H. U. Güdel and A. Ludi, *Chem. Phys. Lett.*, 1979, **62**, 153–157.

20 S. Decurtins, F. Felix, J. Ferguson, H. U. Güdel and A. Ludi, *J. Am. Chem. Soc.*, 1980, **102**, 4102–4106.

21 P. Gütlich, A. Hauser and H. Spiering, *Angew. Chem., Int. Ed.*, 1994, **33**, 2024–2054.

22 S. K. Hain, F. W. Heinemann, K. Gieb, P. Müller, G. Hörner and A. Grohmann, *Eur. J. Inorg. Chem.*, 2010, **2010**, 221–232.

23 P. Guionneau, M. Marchivie, G. Bravic, J.-F. Létard and D. Chasseau, in *Spin Crossover in Transition Metal Compounds II*, ed. P. Gütlich and H. A. Goodwin, Springer, Berlin, 2004, pp. 97–128.

24 M. Sorai and S. Seki, *J. Phys. Chem. Solids*, 1974, **35**, 555–570.

25 P. Guionneau, C. Brigouleix, Y. Barrans, A. E. Goeta, J.-F. Létard, J. A. K. Howard, J. Gaultier and D. Chasseau, *C. R. Acad. Sci., Ser. IIc: Chim.*, 2001, **4**, 161–171.

26 H. Zabrodsky, S. Peleg and D. Avnir, *J. Am. Chem. Soc.*, 1992, **114**, 7843–7851.

27 S. Alvarez, *J. Am. Chem. Soc.*, 2003, **125**, 6795–6802.

28 W. L. F. Armarego and C. L. L. Chai, *Purification of Laboratory Chemicals*, Butterworth-Heinemann, Oxford, 5th edn, 2003.

29 E. A. Ünal, D. Wiedemann, J. Seiffert, J. P. Boyd and A. Grohmann, *Tetrahedron Lett.*, 2012, **53**, 54–55.

30 G. R. Fulmer, A. J. M. Miller, N. H. Sherden, H. E. Gottlieb, A. Nudelman, B. M. Stoltz, J. E. Bercaw and K. I. Goldberg, *Organometallics*, 2010, **29**, 2176–2179.

31 G. A. Bain and J. F. Berry, *J. Chem. Educ.*, 2008, **85**, 532–536.

32 Agilent Technologies, *CrysAlisPro: Intelligent Data Collection and Processing Software for Small Molecule and Protein Crystallography*, Agilent Technologies Ltd., Oxford, United Kingdom, 2013.

33 G. M. Sheldrick, *Acta Crystallogr., Sect. A: Found. Crystallogr.*, 2008, **64**, 112–122.

34 L. J. Farrugia, *J. Appl. Crystallogr.*, 1997, **30**, 565.

35 C. F. Macrae, I. J. Bruno, J. A. Chisholm, P. R. Edgington, P. McCabe, E. Pidcock, L. Rodriguez-Monge, R. Taylor, J. van de Streek and P. A. Wood, *J. Appl. Crystallogr.*, 2008, **41**, 466–470.

36 L. J. Farrugia, *J. Appl. Crystallogr.*, 1999, **32**, 837–838.

37 A. L. Spek, *Acta Crystallogr., Sect. D: Biol. Crystallogr.*, 2009, **65**, 148–155.

38 R. S. Bubnova, V. A. Firsova and S. K. Filatov, *Glass Phys. Chem.*, 2013, **39**, 347–350.

39 A. Zayit, M. Pinsky, H. Elgavi, C. Dryzun and D. Avnir, *Chirality*, 2011, **23**, 17–23.